AGU PUBLICATIONS

JGR

Journal of Geophysical Research: Space Physics

RESEARCH ARTICLE
10.1002/2016JA022912

Key Points:
- Long-term survey of plasma waves at frequencies 1–10 kHz inside Saturn's foreshock
- High activity of narrowband emissions maps the entire upstream region at Saturn
- Less intense and more complex waves are observed deeper inside the foreshock

Correspondence to:
D. Píša,
dp@ufa.cas.cz

Citation:
Píša, D., O. Santolík, G. B. Hospodarsky, W. S. Kurth, D. A. Gurnett, and J. Souček (2016), Spatial distribution of Langmuir waves observed upstream of Saturn's bow shock by Cassini, *J. Geophys. Res. Space Physics*, *121*, 7771–7784, doi:10.1002/2016JA022912.

Received 5 MAY 2016
Accepted 30 JUL 2016
Accepted article online 4 AUG 2016
Published online 25 AUG 2016

Spatial distribution of Langmuir waves observed upstream of Saturn's bow shock by Cassini

D. Píša[1,2], O. Santolík[2,3], G. B. Hospodarsky[1], W. S. Kurth[1], D. A. Gurnett[1], and J. Souček[2]

[1]Department of Physics and Astronomy, University of Iowa, Iowa City, Iowa, USA, [2]Institute of Atmospheric Physics CAS, Prague, Czech Republic, [3]Faculty of Mathematics and Physics, Charles University in Prague, Prague, Czech Republic

Abstract We present the spatial distribution and spectral properties of Langmuir waves observed upstream of Saturn's bow shock by the Cassini spacecraft. The entire 10 kHz wideband data set obtained between June 2004 and December 2014 has been analyzed using an automated procedure. Almost 10^6 waveform snapshots with intense narrowband emissions in the frequency range of 1–10 kHz were detected. A typical wave spectrum exhibits a single intense peak (62% of all selected waveforms). However, spectra with a superposition of two (25%) or more (13%) intense peaks are also observed. Using magnetic field observations and a model of the bow shock, plasma wave activity across Saturn's foreshock has been mapped. The plasma wave occurrence increases steeply behind the tangent magnetic field line, i.e., the sunward foreshock boundary, and rises with increasing distance from the tangential line into the downstream region. The single peak spectra are observed across the entire foreshock, while more complicated spectra are more likely measured deeper inside the foreshock and closer to the bow shock. We confirm that the most intense waves occur close to the tangent point and decrease both deeper in the foreshock and along the tangential line.

1. Introduction

Electron plasma oscillations, also known as Langmuir waves, are common emissions observed in regions upstream of planetary and interplanetary shocks. Solar wind electrons accelerated at the shock front are reflected back into the solar wind forming electron beams, which stream along the solar wind magnetic field lines. In regions containing these electron beams, usually called the electron foreshock [e.g., *Russell and Hoppe*, 1983; *Fitzenreiter*, 1995], the electron distribution becomes unstable and electrostatic Langmuir waves are generated via the beam instability [e.g., *Scarf et al.*, 1971]. The wave intensity and spectral properties depend strongly on the position inside the foreshock.

In a relatively narrow region behind the leading magnetic field line tangent to the bow shock, Langmuir waves are most intense [*Filbert and Kellogg*, 1979; *Cairns et al.*, 1997]. Close to this upstream boundary, waves are usually observed as narrowband emissions with single peak spectra at a frequency close to the electron plasma frequency, f_p [*Etcheto and Faucheux*, 1984]. Deeper downstream, waves are often more complex showing a wide frequency spread with upshifted or downshifted emissions [*Lacombe et al.*, 1985; *Fuselier et al.*, 1985]. These complicated spectra often have the form of the superposition of two or more spectral peaks. It is believed that these spectra result from the Doppler shift of back-scattered waves, plasma density inhomogeneities [*Smith and Sime*, 1979; *Krasnoselskikh et al.*, 2011; *Krafft et al.*, 2014; *Voshchepynets et al.*, 2015], or nonlinear three-wave interactions of two Langmuir waves with ion acoustic or transverse electromagnetic waves [*Robinson*, 1995; *Bale et al.*, 2000; *Soucek et al.*, 2005; *Graham and Cairns*, 2013, 2014, and reference therein]. The presence of Langmuir waves has been reported in the upstream region of all planets from Venus to Neptune observed by a number of spacecraft including Voyager 1 and 2 [*Gurnett et al.*, 1981; *Scarf et al.*, 1982; *Gurnett et al.*, 1986, 1992], Galileo [*Hospodarsky et al.*, 1994], Cassini [*Hospodarsky et al.*, 2006; *Píša et al.*, 2015], Cluster [*Soucek et al.*, 2003; *Sigsbee et al.*, 2004], Wind [*Bale et al.*, 1997], and STEREO [*Malaspina et al.*, 2009].

The first systematic study of Langmuir wave activity was done for Venus' foreshock [*Crawford et al.*, 1993]. Measurements from the Pioneer Venus Orbiter showed the highest wave intensity close to the leading foreshock boundary and strong decrease of the wave intensity for distances beyond $\sim 15\, R_V$ from the tangent point along the foreshock boundary [*Crawford et al.*, 1998]. An extensive mapping of the terrestrial foreshock

was done using ISEE-3 [*Fitzenreiter*, 1995], Geotail [*Kasaba et al.*, 2000], and STEREO [*Malaspina and Ergun*, 2008] observations. Langmuir wave activity connected to Earth's bow shock has been detected at distances up to ~250 R_E [*Greenstadt et al.*, 1995; *Malaspina et al.*, 2009], relatively much further than at Venus. The difference in Langmuir wave activity inside both foreshocks can be explained by the curvature of the shock that significantly controls the energization processes [*Strangeway*, 2004].

There is also a strong asymmetry of wave activity observed in the sunward and antisunward region of the foreshock with a visible gap between both regions at Venus. This asymmetry was not clearly identified at Earth by the Geotail observations [*Kasaba et al.*, 2000]. However, *Pulupa et al.* [2011] presented new results from Wind observations and reported evidence of such an asymmetry. One possible explanation of the wave activity asymmetry is based on the contribution of high energy strahl electrons to an unstable electron distribution function.

Reports of statistical observations of Langmuir waves inside the foreshock of outer planets, such as Saturn, are currently limited. After the orbit insertion in June 2004, the Cassini spacecraft occasionally leaves Saturn's magnetosphere and enters the solar wind. Cassini spent more than 18 months total observation time in the solar wind beyond Saturn's bow shock from June 2004 to 2014, allowing a comprehensive study of Langmuir waves at Saturn to be performed. At Saturn's orbit (~10 AU), the solar wind density is about 2 orders of magnitude lower than at Earth and the typical Parker spiral angle increases from ~45° at Earth to ~90° at Saturn. These plasma parameters result in a high Mach number quasiperpendicular shock at Saturn [*Sulaiman et al.*, 2015], where the Mach number is defined as the ratio of the flow speed to a characteristic wave speed. For a quasiperpendicular shock, the angle, θ_{Bn}, between the solar wind magnetic field direction and normal to the shock front is greater than 45°. The semiempirical bow shock model of *Went et al.* [2011] obtained from almost 600 bow shock crossings gives an averaged subsolar stand off distance of 28 R_S. The first systematic analysis of Langmuir wave amplitudes at Saturn [*Píša et al.*, 2015] shows that typical wave amplitudes are in the range of 0.01 – 1 mV/m. The amplitude distribution follows a log normal distribution with a power law tail for amplitudes greater than 1 mV/m. The amplitude intensity has an onset behind the leading foreshock boundary and falls off with increasing depth into the downstream and distance along the magnetic field line.

In this paper, we present a systematic study of the spatial distribution of Langmuir waves inside Saturn's foreshock. All available wideband data from the Radio and Plasma Wave Science (RPWS) instrument [*Gurnett et al.*, 2004] on board the Cassini spacecraft from 2004 to 2014 were analyzed. Using the interplanetary magnetic field measurements and the *Went et al.* [2011] model of the bow shock, we have mapped Langmuir wave activity in Saturn's foreshock. Plasma oscillations are mostly observed within a narrow region of the electron foreshock. Deeper inside the ion foreshock more complex emissions including also beam and acoustic wave modes [e.g., *Gary*, 1985] are observed. We do not distinguish between the electron and ion foreshock [*Russell and Hoppe*, 1983], and we analyze only intense narrowband emissions in this study.

2. Data

The analyzed data set was restricted to spacecraft periods outside Saturn's bow shock between June 2004 and December 2014. To recognize these positions, a list of Cassini bow shock crossings provided by the MAPSview group (http://mapsview.engin.umich.edu) was used. The crossings were visually identified by changes in the magnetic field strength and the plasma density and temperature [*Masters et al.*, 2008]. One component of the electric field obtained by the Wideband receiver (WBR), a part of the Radio and Plasma Wave Science (RPWS) instrument, has been processed over a bandwidth of 60 Hz to 10.5 kHz. The WBR observations are not continuous and typically last up to 3 min. During this time period, the waveform is sampled at a frequency of 27.8 kHz. Each interval is typically broken in snapshots with lengths of either 37 or 74 ms. This study only uses waveform snapshots with a length of either 37 or 74 ms, which is almost 84% of total WBR waveform snapshots measured beyond the bow shock. Due to an automated gain control the WBR dynamic range is almost 120 dB. However, the gain is updated only once per waveform snapshot; hence, occasional clipping of the signal still occurs. Clipped waveforms were not considered in the study. An example of time-frequency spectrogram with the Langmuir waves signature observed inside Saturn's foreshock on 27 June 2004 calculated from the WBR observations is shown in Figure 1.

The strength and direction of the interplanetary magnetic field (IMF) were obtained from the triaxial fluxgate magnetometer which is a part of the magnetometer (MAG) instrument [*Dougherty et al.*, 2004]. Data with a 1 s

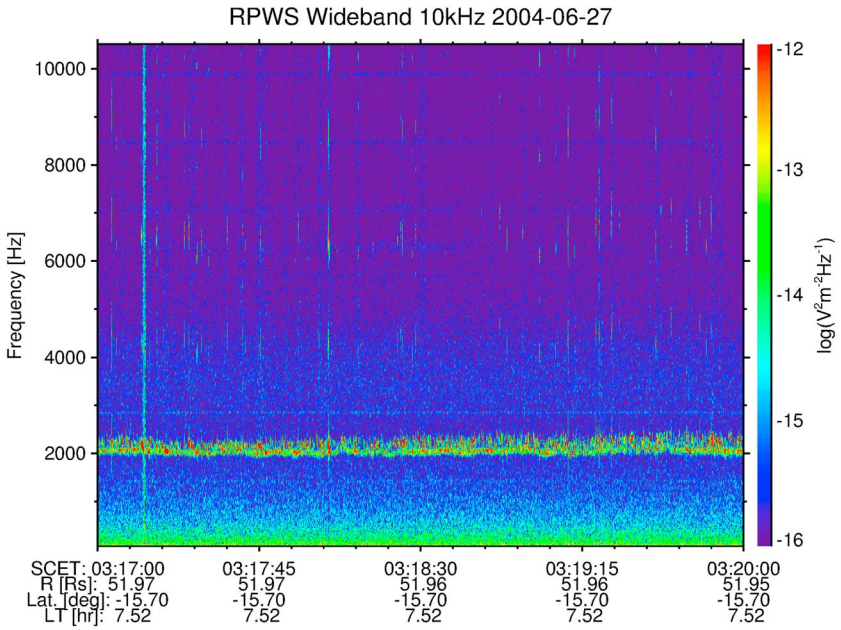

Figure 1. An example of a time-frequency spectrogram for one electric component with the Langmuir waves signature measured by the RPWS Wideband receiver on board Cassini outside of Saturn's bow shock.

sampling cadence were used and smoothed using a 1 min window to exclude high frequency perturbations that do not contribute to the overall of the foreshock and that would cause an inaccurate estimate of the IMF direction. The IMF data are transformed into the Kronian Solar Orbital (KSO) coordinate system. This system is defined such that the *X* axis points directly to the Sun, the *Y* axis lies in the orbital plane of Saturn and is positive in the dusk direction, and the *Z* axis completes the orthogonal system. The magnetic field observations are then rotated around the *X* axis into a plane of constant *Z* equals 0. For each WBR waveform snapshot, the average azimuthal angle, i.e., angle between the solar wind direction and the IMF rotated into the orbital plane, and its standard deviation have been calculated. The distribution of these average azimuthal angles projected into the dusk half plane and their standard deviations obtained during the WBR observation periods beyond the bow shock are shown in Figures 2a and 2b, respectively. The red line in Figure 2a represents a Gaussian fit with a mean value of 90 and half width of 19°. Positions with azimuthal angles less than 65° or greater than 115° and with standard deviations greater than 5° were excluded from further calculations of foreshock positions (Figure 2b). The median value of the remaining distribution of standard deviations is 1.8°. Larger variations in the magnetic field orientation can significantly increase inaccuracy in a foreshock position calculation.

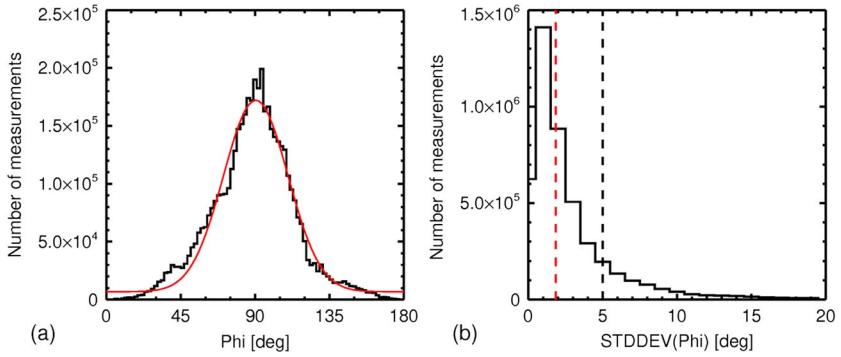

Figure 2. (a) Distribution of the 1 min averaged angles between the solar wind direction and the interplanetary magnetic field rotated into the orbital plane ($Z_{KSO=0}$) for all WBR measurements beyond the bow shock. (b) Distribution of standard deviations estimated for the azimuthal angles within the 1 min window. The black dashed lines represent standard deviation equal to 5°. The red dashed line shows the mean uncertainty of the azimuthal angles used in the study equal to 1.8°.

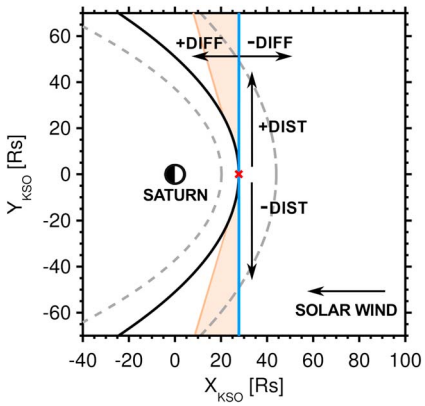

Figure 3. Geometry of the Saturn's electron foreshock (orange color) in KSO coordinates for an 90° angle between the solar wind direction and interplanetary magnetic field (blue solid line). The gray dotted line indicates the lower and upper limit of the bow shock position obtained by the *Went et al.* [2011] model. The bow shock position used in the study is shown by the black solid line. The red cross defines the position of the tangent point.

Using the measured IMF directions and model of the bow shock, more than 2×10^6 positions of WBR measurements have been converted into the foreshock coordinate system [*Filbert and Kellogg*, 1979; *Cairns and Robinson*, 1997]. The geometry of Saturn's electron foreshock (orange region) projected into the orbital plane in KSO coordinates is shown in Figure 3. The blue solid line is the IMF direction, shown here for a Parker angle of 90°. The gray dashed lines present the lower and upper limit of the bow shock position obtained by the *Went et al.* [2011] model for dynamic pressures of 0.2 and 0.003 nPa, respectively. The bow shock position for the average solar wind dynamic pressure of 0.036 nPa, which is used in the study, is shown by the black solid line. The red cross defines the tangent point of a magnetic field line to the bow shock. Assuming the solar wind direction is parallel to the X_{KSO} axis, the DIFF coordinate is positive along the X_{KSO} axis in the downstream direction measured from the tangent magnetic field line. The DIST coordinate is measured a along the tangential field line from the tangent point to the closest point on the tangential field line to the spacecraft position. The sign of the DIST coordinate indicates the dawnward (−) or duskward (+) sector of the foreshock region [*Pulupa et al.*, 2011].

There are several simplifications which result in uncertainty in the foreshock position estimates. First, the average position and shape of the bow shock have been used. This is because there is no solar wind monitor ahead of Saturn and Cassini's observations of the solar wind speed and particle density are limited. The average solar wind velocity was obtained from the first 7 months (June 2004–January 2005) of Cassini's Magnetospheric IMaging Instrument (MIMI) solar wind velocity data from the MAPSview site (http://mapsview.engin.umich.edu). The average density was calculated using the frequency of the detected Langmuir wave emissions. The experimental uncertainty of the foreshock position was determined using the Monte Carlo method. The overall uncertainty is estimated using uncertainties in the values of the bow shock parameters ($c_1 = 15 \pm 1$, $c_2 = 5.4 \pm 0.5$, and $\epsilon = 0.84 \pm 0.06$) obtained from *Went et al.* [2011], the solar wind speed of $v_{sw} = 445 \pm 54$ km/s, constant plasma density of $n = 0.11$ cm^{-3} from the observed mean plasma frequency (2932 Hz) and the averaged magnetic field direction of 90° with a standard deviation 1.8° from the MAG observations. The calculated DIFF coordinate and its experimental error as a function of the $X - Y_{KSO}$ position are shown in Figure 4. For each position, 10,000 foreshock positions were generated using all parameters with normally distributed deviations. A distribution of mean DIFF positions is presented in Figure 4a. The black contour shows the mean position of the tangent field line, i.e., DIFF = 0 R_S. The standard deviation of the DIFF coordinate estimates is plotted in Figure 4b. The model of the bow shock for a solar wind dynamic pressure of 0.036 nPa is plotted by the black dashed line. One can see that the uncertainty of foreshock depth is typically 2–3 R_S around the tangent point and varies up to ~5 R_S for larger distances.

Another simplification is that the upstream foreshock boundary is defined as the straight line traced by an electron reflected from the bow shock with infinite velocity. The actual foreshock region is formed by the path of the fastest beam electron path. In reality, the onset of wave activity is curved downstream at larger distances from the tangent point. For an electron beam of ≤1 keV, solar wind speed of 445 km/s, and an IMF orientation of 90°, the onset of wave activity is shifted by ~2.5 R_S into the downstream at a distance of 100 R_S from the tangent point. An additional error is due to the assumption that the IMF tangent line is a straight line connecting the tangent point and satellite [*Zimbardo and Veltri*, 1996]. Due to facts mentioned above and results in Figure 4b, uncertainties are estimated to be smaller (<2 R_S) close to the tangent point but become larger than 5 R_S at greater distances (>70 R_S) from the tangent point.

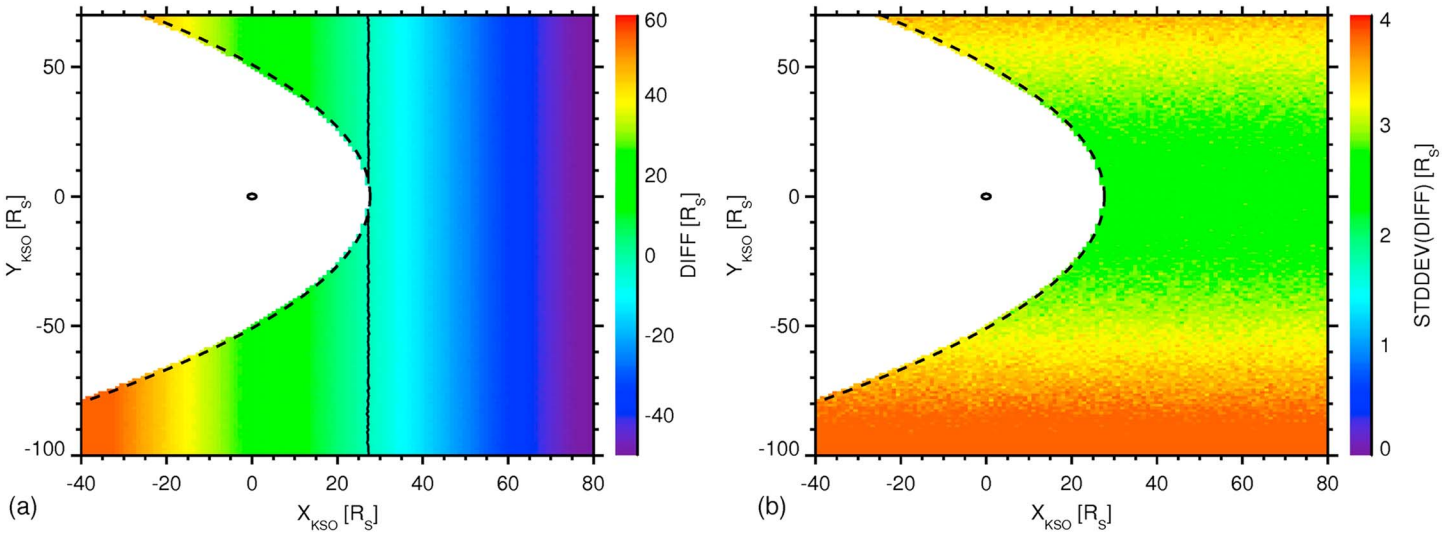

Figure 4. Simulation of foreshock positions using the Monte Carlo method. (a) Distribution of calculated DIFF coordinates as a function of the $X - Y_{KSO}$ positions. The black solid contour shows the mean position of the tangent field line, DIFF = 0 R_S. (b) Distribution of the experimental uncertainties for the DIFF coordinate estimates. The bow shock position for a dynamic pressure of 0.036 nPa is shown by the black dashed line.

3. Method

Between July 2004 and December 2014 Cassini spent more than 500 days beyond Saturn's bow shock and made more than 5.7×10^6 WBR measurements. All solar wind visits were during low inclination orbits within 20 R_S from Saturn's orbital plane. Initially, all waveform snapshots were checked for clipping and duration. There were $\sim 4 \times 10^4$ (0.7%) waveform snapshots clipped and almost 9×10^5 (16%) truncated snapshots during the analyzed period. The remaining unclipped WBR waveform snapshots with a length of 1024 or 2048 samples ($\sim 4.6 \times 10^6$ snapshots) were calibrated, and their power spectra were calculated using a fixed Fast Fourier Transform (FFT) window with a length of 512 samples (~18.4 ms) and 50% overlap, i.e., three or five spectra averaged together. This setting gives a frequency resolution of about 54 Hz.

In the next step of the procedure a maximum and median wave power within the frequency range of 1–10 kHz are found. The maximum peak power has to be a factor of 50 (~17 dB) or greater than the median wave power within the frequency range of 1–10 kHz to be selected for the next step of determining a peak boundary. For this purpose a spectrum derivative using the three-point Lagrangian interpolation is done. The peak boundary is identified from changes in the sign of the derivative. If there is no change in the derivative sign on one side of the spectrum, the boundary is set to either 1 or 10 kHz. The background noise level at the peak boundary is estimated for both sides of the peak and compared with the peak intensity. If the peak intensity is a factor of 50 (~17 dB) or greater than the background level at the peak boundaries then the wave peak is selected. Otherwise, the procedure looks for further derivative changes. If a peak with sufficient intensity is not found after five derivative changes on both sides, then no peak is selected. The selected peak is fitted by a Gaussian function using a nonlinear least squares fit. The fitted part of the spectrum is then subtracted and the procedure continues searching for the next intense peak. The peak selection is repeated until the whole spectrum is inspected or until the last identified peak has an intensity ≤ -30 dB compared to the overall maximum peak intensity between 1 and 10 kHz.

Examples of selected WBR spectra are plotted in Figure 5. Figure 5a presents the most typical spectral shape with one intense peak. More complicated spectra composed of two or more peaks are shown in Figures 5b–5d.

4. Systematic Analysis

The results of a survey of the positions of Langmuir wave events observed between June 2004 and December 2014 projected onto the KSO equatorial plane are shown in Figure 6 with a spatial resolution of $4 \times 4\,R_S$. Figure 6a represents the number of WBR waveforms measured during the inspected time period outside the bow shock. The black arrow shows the first inbound orbit to the Saturnian system in June 2004 before

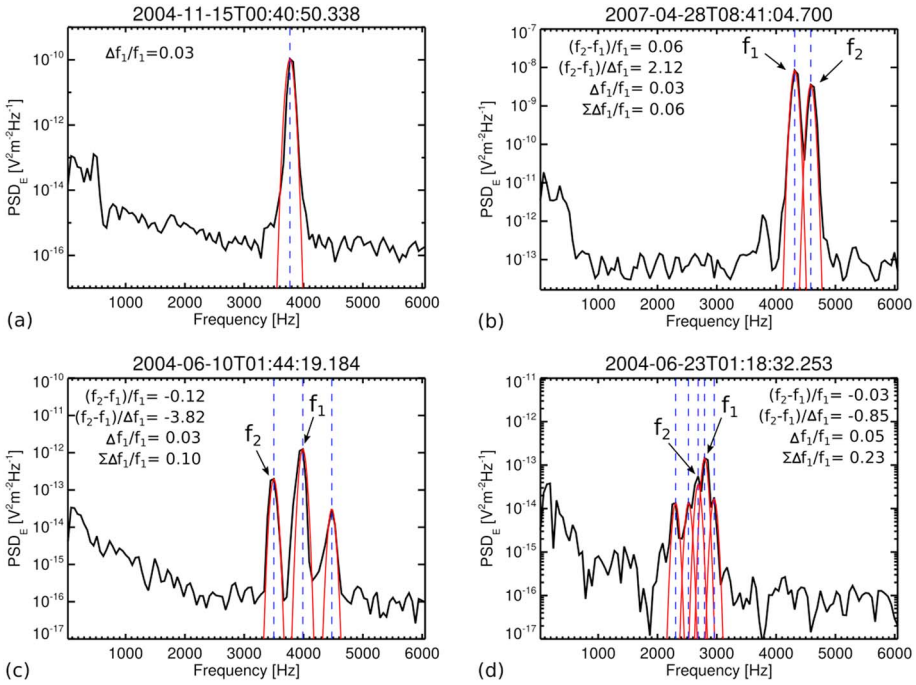

Figure 5. Examples of spectra with Langmuir wave signatures selected by an automated procedure (described in section 3). Spectra with (a) one and (b) two intense peaks. More complicated spectra with (c) three and (d) five detected peaks. The blue dashed line represents the frequency of the peak. The Gaussian fit for each detected peak is plotted by a red solid line. A detailed explanation of parameters shown in each panel is presented in section 4.

the orbit insertion. The occurrence rate of narrowband plasma waves as a function of position is plotted in Figure 6b. The black dashed line represents the *Went et al.* [2011] bow shock model discussed above. The black dotted line shows the lower and upper limits for the bow shock positions using the same model for the dynamic pressure equal to 0.2 and 0.003 nPa, respectively. The position of Saturn is indicated by the black circle. The first evidence of plasma oscillations related to an interaction of the solar wind with Saturn's magnetosphere was encountered early in June 2004 at distances of about 250 R_S from the planet. While the spacecraft was approaching Saturn, sporadic WBR measurements of plasma waves became more common, sometimes exceeding an occurrence rate of 50%. During the first 2 years, the spacecraft had several excursions

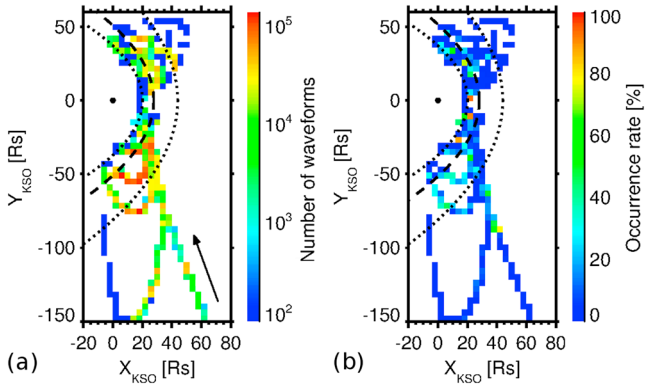

Figure 6. Results of the Langmuir wave survey for 2004 through 2014 in a spatial grid of $4 \times 4\,R_S$. (a) Number of WBR waveforms captured beyond the bow shock as a function of the $X - Y_{KSO}$ position. (b) Occurrence rate of Langmuir waves observed outside Saturn's bow shock as a function of position in the $X - Y_{KSO}$ plane. The black dashed line represents the position of the bow shock used in the study for a dynamic pressure of 0.036 nPa calculated from the *Went et al.* [2011] model. The black dotted lines show the lower and upper limits for the foreshock position using the same model for a dynamic pressure of 0.2 and 0.003 nPa, respectively. The black arrow shows Cassini's trajectory before entering orbit around Saturn which is indicated by the black circle.

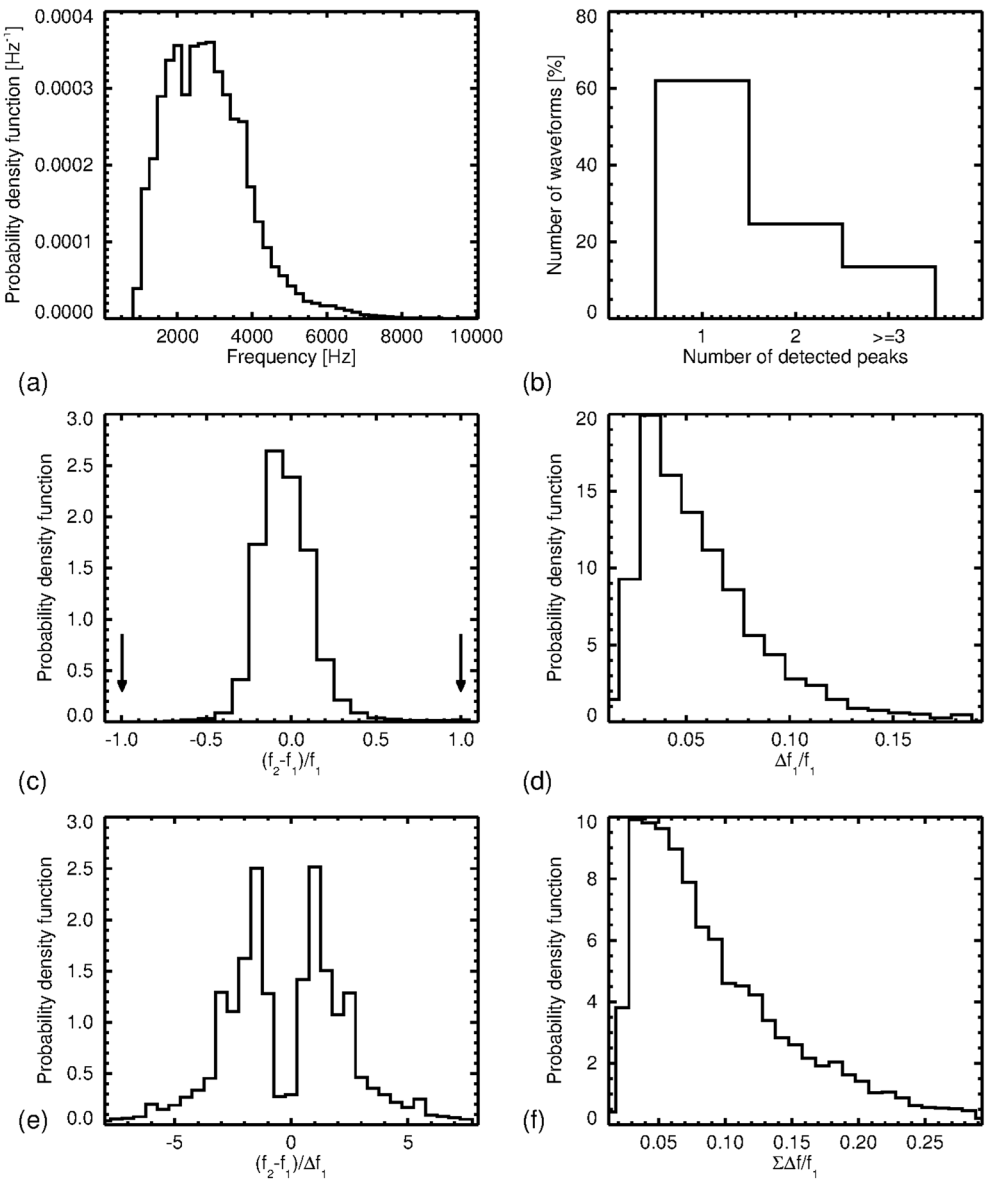

Figure 7. (a) Distribution of frequencies for the most powerful spectral peak in WBR snapshots for Langmuir waves beyond the bow shock. (b) Number of peaks detected in each selected snapshot. (c) Normalized difference of frequencies for the second and first detected peak. The black arrows show positions of the second harmonics. (d) The spectral width of the first peak normalized by the peak frequency. (e) Distribution of frequency differences of the second and first peak normalized by the spectral width of the first peak. (f) Sum of the spectral widths for all peaks detected in a snapshot normalized by the frequency of the most intense peak.

into the solar wind mostly in the dawn local time sector ($-Y_{KSO}$). Later in the mission, there were several solar wind visits in the dusk sector ($+Y_{KSO}$). After 2012 there are only a few short excursions into the solar wind.

Using the automated procedure discussed above, almost 1×10^6 waveform snapshots with intense spectral peaks were selected from the total number of 4.6×10^6 snapshots leading to an overall occurrence rate of ~21%. The distribution of frequencies of the most powerful peak in each selected waveform is plotted in Figure 7a. This distribution shows that the most probable frequency is 2875 Hz; the mean frequency and standard deviation are 2931 Hz and 1127 Hz, respectively. More than 98% of detected waveforms have the most intense spectral peak within the frequency range of 1–6 kHz. The number of peaks detected in each waveform is presented in Figure 7b. More than 62% of all selected events consist of a single intense peak. More complex events, with increasing numbers of peaks, decrease in frequency of occurrence with the number of peaks, reaching of about 13% for spectra with three and more detected peaks. The frequency of the second

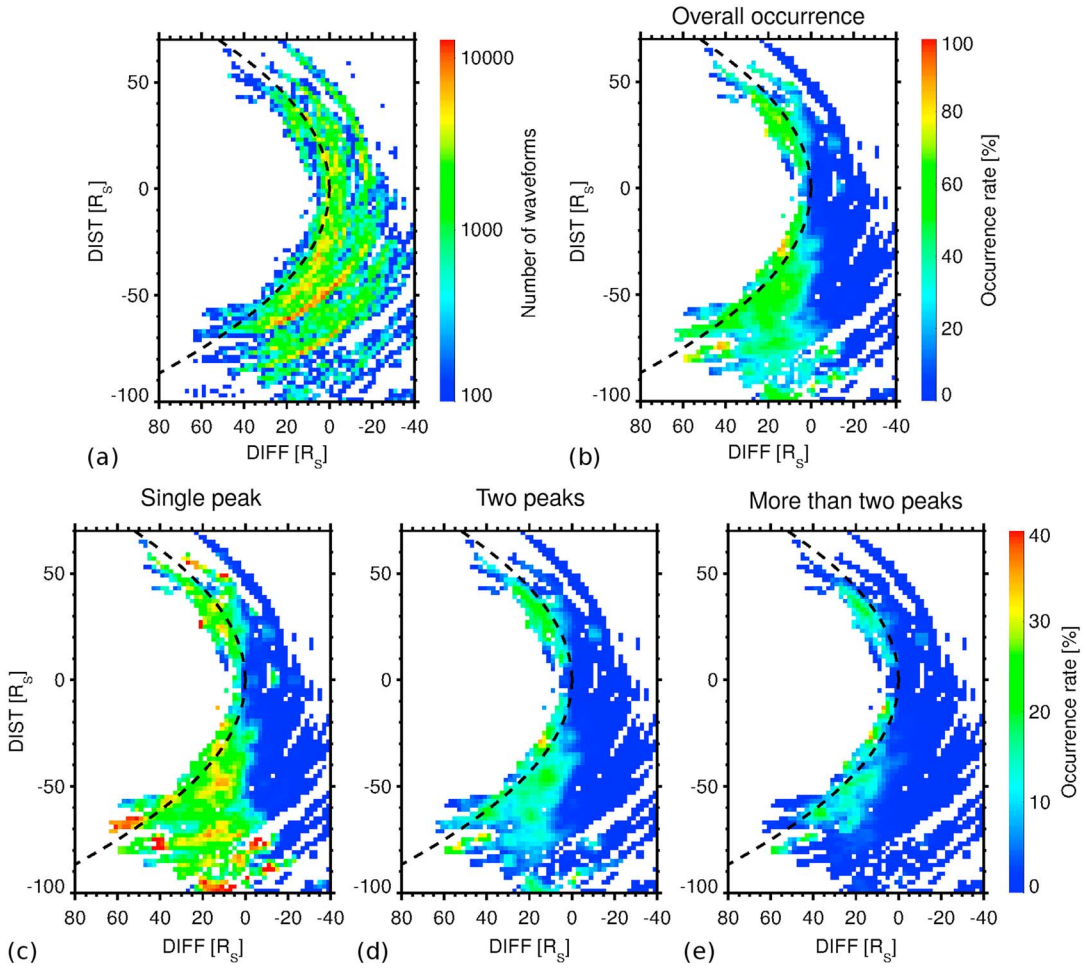

Figure 8. Results of the Langmuir wave survey for 2004 through 2014. (a) Number of WBR waveforms captured beyond the bow shock as a function of foreshock position. (b) Overall occurrence rate of Langmuir waves observed outside Saturn's bow shock as a function of foreshock position. (c–e) Occurrence rates of Langmuir waves with a single peak (61% of all Langmuir waves mapped into the foreshock), two peaks (26%), and more than two peaks (14%), respectively. The black dashed line delimits the position of the bow shock in foreshock coordinates for a dynamic pressure of 0.036 nPa and IMF direction of 90° obtained from the *Went et al.* [2011] model. A 2×2 R_S grid spacing was used. Occurrence maps have been smoothed using a 6×6 R_S box average.

peak is typically close to the first one (Figure 7c) with no pronounced evidence of intense second harmonics (shown by black arrows). For each analyzed snapshot, detected peaks were fitted by a Gaussian function and the spectral widths were calculated. The spectral width is defined as the full width at half maximum from the Gaussian fit. The distribution of the spectral widths normalized by the frequency of the most intense peak (Figure 7d) shows that our analysis is limited from below by the finite relative frequency resolution of our processing (~3%). This finite frequency resolution causes an artificial decrease of the probability density function below the relative width of 3%. Fluctuations in the local electron density and/or finite electron beam temperature cause a spread of the relative widths, for which the occurrence gradually decreases with an increasing relative width up to 15–20% (Figure 7d). Most of the second peaks are within ±3 spectral widths of the first peak (Δf_1) showing that the second peak is often close to the first one (Figure 7e). Figure 7f shows the probability density function of the sum of the spectral widths for all peaks detected in each snapshot. This sum is normalized by the frequency of the largest spectral peak. The occurrence of this normalized sum of the spectral widths shows the same limitations by the finite relative frequency resolution of our analysis (~3%), as it was already discussed in the case of Figure 7d. Obviously, the sum of the spectral widths in Figure 7f shows a larger spread compared to Figure 7d, with a nonnegligible occurrence extending to higher values (up to 25%). All calculated parameters for typical spectra are shown in Figure 5.

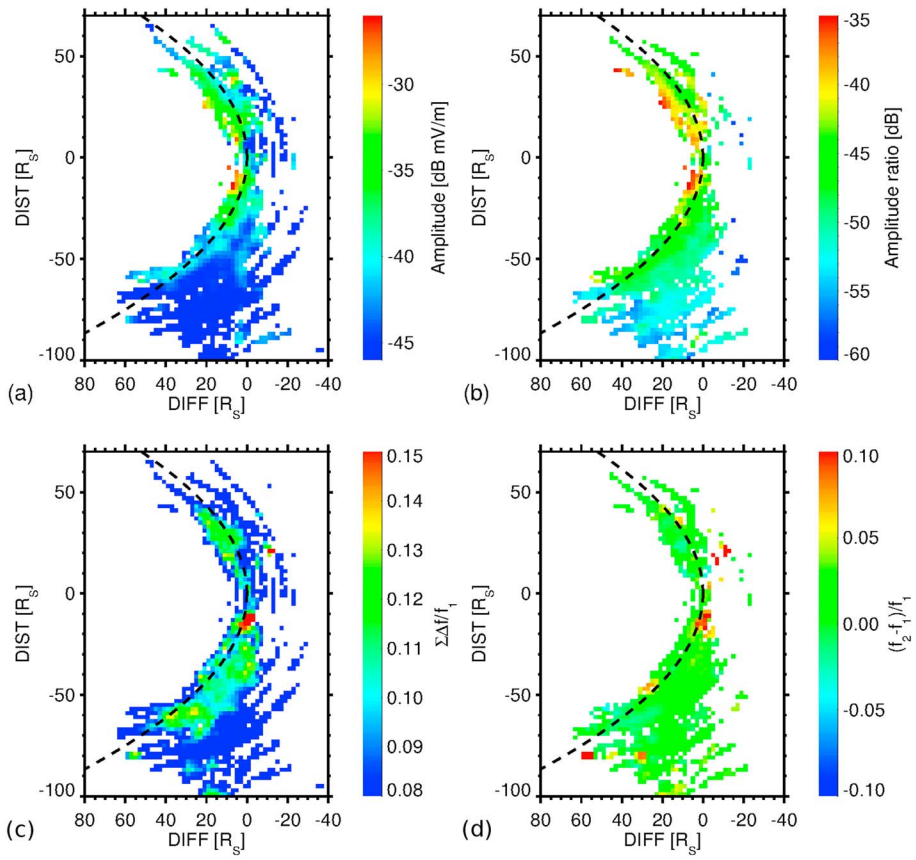

Figure 9. (a) Distribution of amplitudes for all WBR observations with detected Langmuir waves as a function of foreshock position in the smoothed 2×2 R_S spatial grid. (b) Distribution of the ratio of amplitudes for the first and second detected peak in a waveform snapshot. (c) The sum of the spectral widths normalized by the frequency of the most intense peak in a snapshot. (d) Normalized frequency difference of the second and first peak. The black dashed line represents the position of the bow shock model for an IMF direction of 90° and solar dynamic pressure of 0.036 nPa.

All WBR data obtained during time periods of unperturbed interplanetary magnetic field ($\sigma_{PHI} < 5°$) and with absolute values of the azimuthal angle between 65 and 115° with respect to the solar wind direction were mapped into the foreshock coordinate system. This reduces the original number of 9.5×10^5 detected snapshots down to 5.8×10^5 (~61%) WBR snapshots gathered across the foreshock with a spatial resolution of 2×2 R_S between June 2004 and December 2014 (Figure 8a). The occurrence rate versus position for almost 5.8×10^5 snapshots including Langmuir waves is plotted in Figure 8b with a spatial resolution of $2 \times 2\,R_S$. Occurrence rates were smoothed using a $6 \times 6\,R_S$ box averaging. Positions with less than 10 data points are excluded. The occurrence rate within the DIST interval of $\pm 50\,R_S$ shows a visible leading edge (DIFF = 0). Behind this boundary, there is a steep increase of wave occurrence rate reaching on average 39% for all data with DIFF > 0 R_S. For DIST positions < −70 R_S in the region with DIFF > 0, the occurrence rate is still on average of 36%. However, this high occurrence region is also spread to negative DIFF positions, i.e., in front of the leading foreshock boundary. This is caused by the uncertainty in the DIFF estimates at larger DIST. Figure 8 also shows the occurrence rate as a function of foreshock positions for (Figure 8c) single (61% of all mapped snapshots with Langmuir waves), (Figure 8d) double (26%), and (Figure 8e) multipeak spectra (14%). The single peak spectra are detected across the entire foreshock with a steep onset at the foreshock boundary and a slight increase with increasing DIFF. The double-peak spectra are detected with a lower rate at the leading foreshock boundary and with increasing frequency deeper downstream. Higher occurrence rates for more complicated spectra composed of three and more peaks are found close to the bow shock.

The fits of the most intense peaks in each selected spectrum give the distribution of wave amplitudes as a function of the foreshock position (Figure 9a). As was previously reported [e.g., *Cairns et al.*, 1997] the most intense Langmuir waves are detected close to the tangent point (DIFF = 0 and DIST = 0) and in the narrow

region behind the tangent magnetic field line. Our observations show that both the duskside and dawnside wings of the foreshock exhibit the same level of intensity with the a gap (~10 R_S) around the tangent point. The wave intensity gradually decreases for positions with DIST < −50 R_S. Figure 9b shows a ratio of the amplitude of the first to second peak detected in the waveform snapshot. The amplitudes of the second peak are for most of the positions more than 2 orders of magnitude below the amplitudes of the first peak. The most intense second peaks occur close to the bow shock and deeper into the dusk region. Because most of the second peaks are found very close to the first one (Figure 7e), the sum of the spectral widths for all detected peaks in each snapshot is a useful estimate. Figure 9c shows the distribution of the spectral width sums calculated for each spectrum. Broader emissions (width > 10%) are observed close to the bow shock and deeper in the downstream region. The mean normalized difference of the frequency of first and second peak, $(f_2 - f_1)/f_1$, is plotted in Figure 9d. In each foreshock position typically several hundred values with a mean value of ~1% and standard deviation of ~19% are averaged. Thus, the average value of the normalized frequency difference in Figure 9d varies only up to 5% across almost entire foreshock region. This result illustrates the overall distribution of the normalized frequency differences in Figure 7c, which shows that the secondary peaks are detected at frequencies of up to ~50% above or below the frequency of the first peak with the mean value of 1%. The low value of the mean normalized frequency difference indicates that secondary peaks are observed with a similar probability above and below the primary peak in all foreshock regions; no region dominated by either upshifted or downshifted emissions has been identified. We have not identified any foreshock region with a high occurrence of second harmonics either.

5. Discussion

Intense plasma waves inside Saturn's foreshock are typically electrostatic Langmuir waves observed in the frequency interval of 1–10 kHz [*Scarf et al.*, 1982]. The lower frequency limit for the algorithm was set to 1 kHz to exclude spacecraft noise and instrumental interference. Narrowband Langmuir waves are powerful emissions inside the electron foreshock. The automated procedure identifies them for a selected intensity threshold. We have visually checked more than 1000 randomly selected events and no false matches were found. One can question our assumptions that most of observed waves are electrostatic Langmuir waves. We are of course unable to rule out the transverse electromagnetic Z mode [*Bale et al.*, 1998] or beam-mode waves [*Gary*, 1985]. However, it is impossible to distinguish between particular wave modes without multicomponent measurements and/or detailed information about the electron beam. This fact does not affect our systematic study.

Figure 6a shows the WBR coverage of Saturn's foreshock. Although the spatial resolution is low (4 × 4 R_S), individual orbits can be recognized. This figure shows relatively poor spatial coverage of the upstream region compared to explorations of the Venusian or terrestrial foreshock [e.g., *Crawford et al.*, 1998; *Kasaba et al.*, 2000]. Due to the Cassini trajectory, the region upstream of the subsolar position of the bow shock (10–12 LT) is not covered. However, this region is usually ahead of the foreshock boundary due to the almost perpendicular orientation of the interplanetary magnetic field. The occurrence rates in the KSO coordinate system plotted in Figure 6b are scattered, and the foreshock region with a higher wave activity is not clearly visible.

A better description of the wave activity across the large portion of the upstream region is given in the foreshock coordinate system. In this coordinate system, Saturn's foreshock can be clearly identified behind the well defined leading edge (DIFF = 0). Behind this edge the wave occurrence rate increases up to 80% at DIFF ~20 R_S and DIST of about ±30 R_S in both the duskside and dawnside of the foreshock with a gap close to the tangent point (DIFF = 0 and DIST = 0). The occurrence rate is still above 50% across the entire mapped foreshock. However, due to the peak intensity threshold of ~17 dB above background noise, the occurrence rates are underestimated, especially for the later part of the mission (after 2005) when interferences from Cassini's reaction wheels increased. For positions with DIST < −70 R_S the higher wave occurrence (>50%) is also spread to positions ahead of the predicted foreshock region (DIFF < 0). This inconsistency is likely caused by the inaccurate position of the bow shock and the direction of the magnetic field. Another possible cause is the assumption of a straight magnetic field line is less valid for larger distances from the tangent point [*Malaspina et al.*, 2009]. Because of the lack of a solar wind monitor at Saturn, we have used the averaged dynamic solar wind pressure as input for the *Went et al.* [2011] bow shock model. Although the subsolar position of the bow shock obtained from this model varies from 20 to 40 R_S as a function of the solar wind dynamic pressure, the average solar dynamic pressure gives acceptable results.

The Langmuir waves detected inside Saturn's foreshock have a typical frequency of ~3 kHz and vary between 1.5 and 6 kHz (Figure 7). These frequencies are in an agreement with previous observations by Voyager 1 and 2 [*Gurnett et al.*, 1981; *Scarf et al.*, 1982]. Close to the upstream boundary, Langmuir waves are typically observed as a narrowband emission with a single peak spectrum at a frequency close to the plasma frequency (f_p) [*Cairns et al.*, 1997]. Deeper downstream, the waves are often broader and spread with upshifted or downshifted emissions in the frequency range from $0.1f_p$ to $1.2f_p$ [*Cairns*, 1989]. Unfortunately, more accurate Cassini measurements of plasma density in the upstream region are unavailable. Therefore, it is not possible to independently determine the local plasma frequency and investigate variations of upshifted and downshifted emissions as a function of foreshock position at Saturn. Figure 9c shows the dependence of the sum of the spectral width on the foreshock position. Spectra with broader peaks (>10%) are detected deeper inside the foreshock with a maximum (~15%) close to the tangential field line at a distance of $\sim 20\,R_S$ from the tangent point. This can be explained by changes in the electron distribution function. Deeper inside the foreshock, the beam speed is lower and the beam temperature is higher. This results in a wider frequency range for observed waves [e.g., *Filbert and Kellogg*, 1979; *Cairns*, 1987].

As can be seen in Figure 8c the single peak spectra are observed across the entire foreshock, while complicated spectra (Figures 8d and 8e) are more likely measured deeper inside the foreshock and closer to the bow shock (Figure 9c). The detection algorithm depends on a Gaussian fit of the detected peak. The peak identification works well for a spectrum with a single intense peak (Figure 5a). For a complicated case (Figure 5d) the internal peak structure ($\Delta f > 108$ Hz) can be identified as another peak (Figure 7e). This is why we classify spectra into three groups. The first group represents the single peak spectra that are commonly observed in a narrow region of the electron foreshock close to the tangent field line [*Cairns et al.*, 1997]. However, due to the automated procedure and higher spectral variations deeper inside the foreshock, these spectra are detected within the entire upstream region. The second and third groups show double and multipeak spectra, respectively. Multipeak spectra and spectra with a peak at the second harmonic of the Langmuir wave frequency may suggest nonlinear wave-wave processes that suppress wave growth. Wave amplitudes (up to 10 mV/m) show that the decay instability is possibly the only nonlinear process inside the Saturn's foreshock [*Píša et al.*, 2015]. Another possible explanation is a resonant interaction of Langmuir waves in a plasma with random density fluctuations, which results in multipeak spectra via a modulation effect [e.g., *Krafft et al.*, 2014]. *Cairns et al.* [1998] mentioned that a multipeak spectrum might be the result of a linear superposition of locally generated waves with other waves that were generated earlier and convected or propagated to the satellite's position. We can speculate that this explanation is the most probable for the wave activity inside Saturn's foreshock. However, a more detailed study at shorter time scales is necessary.

Electromagnetic emissions at the second harmonic of the plasma frequency have been reported in the upstream region of Earth [*Kasaba et al.*, 2000] with a possible source placed at the leading boundary of the foreshock. In 4.6×10^6 analyzed snapshots we have only found about 3000 events spread across the foreshock exhibiting an intense peak and a second peak at its harmonic. Although the threshold for the peak intensity might be restrictive, the total occurrence rate of spectra with harmonics is rare (0.15%) inside Saturn's foreshock (see in Figures 7c and 9d). On the contrary, *Sigsbee et al.* [2010] observed the second harmonic peak for 73% and 90% of waveforms with amplitudes 0.1–22 mV/m and 22–100 mV/m, respectively, inside Earth's foreshock. *Graham et al.* [2014] show that the observed harmonics could be caused by nonlinear currents occurring during the Langmuir wave rectification at the sheath surrounding a spacecraft.

Deeper inside the foreshock, Langmuir waves are often complex showing a wide frequency spread with upshifted or downshifted emissions about the local plasma frequency [e.g., *Fuselier et al.*, 1985]. To analyze these shifted emissions, we have calculated the normalized difference between the first and second peak in a spectrum (Figure 7c). We have not observed any systematic predominance of either upshifted or downshifted secondary spectral peaks in any part of the kronian foreshock (Figure 9d).

For a detailed wave interaction study information about the electron and ion distribution function is necessary. Unfortunately, due to a combination of instrumental field of view and sampling period limitations, it is often difficult to identify the distribution function that is unstable and able to generate these plasma waves. Further analysis of each specific event showing a possible wave-wave interaction is beyond the scope of this paper.

Using an improved identification procedure and a larger data set in the present study compared to *Píša et al.* [2015], we show that the most intense waves occur close to the tangent field line around and near the tangent

point and fade out with positions downstream of the tangential field line and farther from the tangent point along the tangential line (see Figure 9a). The highest amplitudes observed in our study are almost 1 order of magnitude lower in comparison to the previous analysis of *Píša et al.* [2015]. The main reason is that here we do not apply an antenna orientation correction, so the amplitude is calculated only from the detected spectral peak. The amplitudes of the second detected peak are typically more than two orders (∼−40 dB) below the amplitudes of the first peak (Figure 9b). The most intense second peaks occur close to the bow shock and deeper in the dusk region. The observed wave amplitudes are in agreement with previous Voyager observations [*Boshuizen et al.*, 2004] and values expected from the theory of the electrostatic decay threshold at Saturn [*Robinson*, 1995]. It has been suggested that wave activity observed inside a planetary foreshock is primarily controlled by the bow shock scale size and curvature. This is because the bow shock scale parameters limit the effectiveness of the Fast Fermi process, which accelerates reflected solar wind electrons comprising electron beams [*Strangeway*, 2004]. At Venus, a combination of a small bow shock radius of curvature ($R_c \sim 2\ R_V$) and a smaller Parker spiral angle (< 45°) results in a wave activity gap around the tangent point. The Venusian bow shock scale size also controls the spatial extent of wave activity along the tangent field line that exhibits a significant drop-off in intensity for distances $> 7\ R_c$, where R_c is the radius of curvature. On the other hand the terrestrial bow shock radius of curvature is larger (20 R_E). Electrons drifting along the motional electric field (∼25 keV/R_E) in the shock ramp gain energy more effectively before shock curvature become important [*Strangeway and Crawford*, 1995]; thus, wave activity is observed up to ∼12 R_c. Two foreshock regions are also observed at Earth with a gap around the tangent point [*Kasaba et al.*, 2000]. However, there is no significant intensity drop-off along the tangent field line. For Saturn's foreshock, one can see the gap in wave activity close to the tangent point with a size of ∼10 R_S in Figures 8b and 9. The region close to the tangent point where the reflection occurs is very small, and Langmuir waves are not excited there. The radius of curvature of Saturn's shock is almost 50 R_S. For a larger radius of curvature, the wave activity occurs further along the tangent field line. The shock curvature also controls the spatial extent of wave activity. We did not observed any visible drop-off in wave activity across the entire inspected part of Saturn's foreshock for distances up to 2 R_c (see in Figure 8b). If we consider Saturn's shock curvature (50 R_S), the estimated wave activity drop-off could occur beyond 600 R_S (12 R_c).

6. Summary

This work focuses on the spatial and spectral properties of Langmuir waves inside Saturn's foreshock. Using a long term survey from June 2004 to 2014, we have analyzed all available WBR waveforms obtained inside the upstream region and detected almost 1×10^6 waveform snapshots with intense narrowband emissions in the frequency range of 1–10 kHz. Spectra with a single intense peak were identified for 62% of all selected cases. More complicated spectra with a superposition of two or more peaks were observed in 25% and 13% of all detected cases, respectively. The Langmuir wave activity across Saturn's foreshock has been mapped using RPWS plasma wave measurements, magnetic field observations, and the model of the bow shock. The Langmuir wave activity increases steeply behind the tangential magnetic field line and rises with increasing distance from the tangent point along the field line and deeper into the foreshock. The single peak spectra are observed across the entire foreshock, while more complicated spectra are more likely seen deeper inside the foreshock and closer to the bow shock. Waves with the highest amplitude occur behind the tangential field line around the tangent point and fade out with distance behind the tangential line and along the field line. A gap in wave occurrence and intensity at the tangent point delimits two foreshock regions similar to those observed at Venus and Earth. In the case of Saturn's foreshock, this gap is caused by the larger radius of curvature of the shock. Wave activity upstream of the bow shock follows solar wind plasma conditions and the orientation of the interplanetary magnetic field ahead of Saturn and is controlled by the bow shock scale size.

Acknowledgments
The authors are grateful to the CASSINI/MAG team, for their support and for access to magnetometer data. Observations of the electric field experiment RPWS/WBR and the magnetic field instrument MAG on Cassini are available on http://ppi.pds.nasa.gov. We acknowledge the use of the list of Cassini bow shock crossings compiled by A. H. Sulaiman, H. J. McAndrews, S. J. Kanani, A. Masters, and J. C. Cutler. We thank the team of M.E. Hill from Johns Hopkins University Applied Physics Lab for the list of the averaged solar wind speeds obtained by the CHEMS/MIMI instrument. Both lists are available on http://mapsview.engin.umich.edu. This work has been supported by NASA through contract 1415150 with the Jet Propulsion Laboratory, from grants P209/16/16050Y and P209/12/2394 of the Grant Agency of Czech Republic, from Praemium Academiae award, and the MSMT grant LH14010.

References

Bale, S. D., D. Burgess, P. J. Kellogg, K. Goetz, and S. J. Monson (1997), On the amplitude of intense Langmuir waves in the terrestrial electron foreshock, *J. Geophys. Res.*, *102*, 11,281–11,286, doi:10.1029/97JA00938.

Bale, S. D., P. J. Kellogg, K. Goetz, and S. J. Monson (1998), Transverse z-mode waves in the terrestrial electron foreshock, *Geophys. Res. Lett.*, *25*, 9–12, doi:10.1029/97GL03493.

Bale, S. D., D. E. Larson, R. P. Lin, P. J. Kellogg, K. Goetz, and S. J. Monson (2000), On the beam speed and wavenumber of intense electron plasma waves near the foreshock edge, *J. Geophys. Res.*, *105*, 27,353–27,368, doi:10.1029/2000JA900042.

Boshuizen, C. R., I. H. Cairns, and P. A. Robinson (2004), Electric field distributions for Langmuir waves in planetary foreshocks, *J. Geophys. Res.*, *109*, A08101, doi:10.1029/2004JA010408.

Cairns, I. H. (1987), Second harmonic plasma emission involving ion sound waves, *J. Plasma Phys.*, *38*, 179–198, doi:10.1017/S0022377800012502.

Cairns, I. H. (1989), Electrostatic wave generation above and below the plasma frequency by electron beams, *Phys. Fluids B*, *1*(1), 204–213, doi:10.1063/1.859088.
Cairns, I. H., and P. A. Robinson (1997), First test of stochastic growth theory for Langmuir waves in Earth's foreshock, *Geophys. Res. Lett.*, *24*, 369–372, doi:10.1029/97GL00084.
Cairns, I. H., P. A. Robinson, R. R. Anderson, and R. J. Strangeway (1997), Foreshock Langmuir waves for unusually constant solar wind conditions: Data and implications for foreshock structure, *J. Geophys. Res.*, *102*, 24,249–24,264, doi:10.1029/97JA02168.
Cairns, I. H., P. A. Robinson, and N. I. Smith (1998), Arguments against modulational instabilities of Langmuir waves in Earth's foreshock, *J. Geophys. Res.*, *103*, 287–300, doi:10.1029/97JA02871.
Crawford, G. K., R. J. Strangeway, and C. T. Russell (1993), VLF imaging of the Venus foreshock, *Geo. Res. Lett.*, *20*, 2801–2804, doi:10.1029/93GL01258.
Crawford, G. K., R. J. Strangeway, and C. T. Russell (1998), Statistical imaging of the Venus foreshock using VLF wave emissions, *J. Geophys. Res.*, *103*, 11,985–12,004, doi:10.1029/97JA02883.
Dougherty, M. K., et al. (2004), The Cassini magnetic field investigation, *Space Sci. Rev.*, *114*, 331–383, doi:10.1007/s11214-004-1432-2.
Etcheto, J., and M. Faucheux (1984), Detailed study of electron plasma waves upstream of the Earth's bow shock, *J. Geophys. Res.*, *89*, 6631–6653, doi:10.1029/JA089iA08p06631.
Filbert, P. C., and P. J. Kellogg (1979), Electrostatic noise at the plasma frequency beyond the Earth's bow shock, *J. Geophys. Res.*, *84*, 1369–1381, doi:10.1029/JA084iA04p01369.
Fitzenreiter, R. J. (1995), The electron foreshock, *Adv. Space Res.*, *15*, 9–27, doi:10.1016/0273-1177(94)00081-B.
Fuselier, S. A., D. A. Gurnett, and R. J. Fitzenreiter (1985), The downshift of electron plasma oscillations in the electron foreshock region, *J. Geophys. Res.*, *90*, 3935–3946, doi:10.1029/JA090iA05p03935.
Gary, S. P. (1985), Electrostatic instabilities in plasmas with two electron components, *J. Geophys. Res.*, *90*, 8213–8221.
Graham, D. B., and I. H. Cairns (2013), Electrostatic decay of Langmuir/z-mode waves in type III solar radio bursts, *J. Geophys. Res.*, *118*, 3968–3984, doi:10.1002/jgra.50402.
Graham, D. B., and I. H. Cairns (2014), Dynamical evidence for nonlinear Langmuir wave processes in type III solar radio bursts, *J. Geophys. Res. Space Physics*, *119*, 2430–2457, doi:10.1002/2013JA019425.
Graham, D. B., I. H. Cairns, and D. M. Malaspina (2014), Harmonic waves and sheath rectification in type III solar radio bursts, *J. Geophys. Res. Space Physics*, *119*, 723–741, doi:10.1002/2013JA019317.
Greenstadt, E. W., G. K. Crawford, R. J. Strangeway, S. L. Moses, and F. V. Coroniti (1995), Spatial distribution of electron plasma oscillations in the Earth's foreshock at ISEE 3, *J. Geophys. Res.*, *100*, 19,933–19,940, doi:10.1029/95JA01400.
Gurnett, D., et al. (2004), The cassini radio and plasma wave investigation, *Space Sci. Rev.*, *114*(1–4), 395–463, doi:10.1007/s11214-004-1434-0.
Gurnett, D. A., W. S. Kurth, and F. L. Scarf (1981), Plasma waves near Saturn—Initial results from Voyager 1, *Science*, *212*, 235–239, doi:10.1126/science.212.4491.235.
Gurnett, D. A., W. S. Kurth, F. L. Scarf, and R. L. Poynter (1986), First plasma wave observations of Uranus, *Science*, *233*, 106–109, doi:10.1126/science.233.4759.106.
Gurnett, D. A., et al. (1992), Plasma wave observations at Neptune, *Adv. Space Res.*, *12*, 47–54, doi:10.1016/0273-1177(92)90422-T.
Hospodarsky, G. B., D. A. Gurnett, W. S. Kurth, M. G. Kivelson, R. J. Strangeway, and S. J. Bolton (1994), Fine structure of Langmuir waves observed upstream of the bow shock at Venus, *J. Geophys. Res.*, *99*(A7), 13,363–13,371, doi:10.1029/94JA00868.
Hospodarsky, G. B., W. S. Kurth, D. A. Gurnett, P. Zarka, P. Canu, M. K. Dougherty, G. H. Jones, A. Coate, and A. Rymer (2006), Observations of Langmuir waves detected by the Cassini Spacecraft, in *Planetary Radio Emissions VI*, edited by H. O. Rucker, W. Kurth, and G. Mann, pp. 67–79, Acad. Sciences Press, Vienna.
Kasaba, Y., H. Matsumoto, Y. Omura, R. R. Anderson, T. Mukai, Y. Saito, T. Yamamoto, and S. Kokubun (2000), Statistical studies of plasma waves and backstreaming electrons in the terrestrial electron foreshock observed by Geotail, *J. Geophys. Res.*, *105*, 79–104, doi:10.1029/1999JA900408.
Krafft, C., A. S. Volokitin, V. V. Krasnoselskikh, and T. D. de Wit (2014), Waveforms of Langmuir turbulence in inhomogeneous solar wind plasmas, *J. Geophys. Res.*, *119*, 9369–9382, doi:10.1002/2014JA020329.
Krasnoselskikh, V. V., T. Dudok, T. D. de Wit, and S. D. Bale (2011), Determining the wavelength of Langmuir wave packets at the Earth's bow shock, *Ann. Geophys.*, *29*, 613–617, doi:10.5194/angeo-29-613-2011.
Lacombe, C., A. Mangeney, C. C. Harvey, and J. D. Scudder (1985), Electron plasma waves upstream of the Earth's bow shock, *J. Geophys. Res.*, *90*, 73–94, doi:10.1029/JA090iA01p00073.
Malaspina, D. M., and R. E. Ergun (2008), Observations of three-dimensional Langmuir wave structure, *J. Geophys. Res.*, *113*, A12108, doi:10.1029/2008JA013656.
Malaspina, D. M., B. Li, I. H. Cairns, P. A. Robinson, Z. Kuncic, and R. E. Ergun (2009), Terrestrial foreshock Langmuir waves: STEREO observations, theoretical modeling, and quasi-linear simulations, *J. Geophys. Res.*, *114*, A12101, doi:10.1029/2009JA014493.
Masters, A., N. Achilleos, M. K. Dougherty, J. A. Slavin, G. B. Hospodarsky, C. S. Arridge, and A. J. Coates (2008), An empirical model of Saturn's bow shock: Cassini observations of shock location and shape, *J. Geophys. Res.*, *113*, A10210, doi:10.1029/2008JA013276.
Píša, D., G. B. Hospodarsky, W. S. Kurth, O. Santolík, J. Souček, D. A. Gurnett, A. Masters, and M. E. Hill (2015), Statistics of langmuir wave amplitudes observed inside Saturn's foreshock by the Cassini spacecraft, *J. Geophys. Res.*, *120*(4), 2531–2542, doi:10.1002/2014JA020560.
Pulupa, M. P., S. D. Bale, and C. Salem (2011), An asymmetry of the electron foreshock due to the strahl, *Geophys. Res. Lett.*, *38*, L14105, doi:10.1029/2011GL048029.
Robinson, P. A. (1995), Stochastic wave growth, *Phys. Plasmas*, *2*, 1466–1479, doi:10.1063/1.871362.
Russell, C. T., and M. M. Hoppe (1983), Upstream waves and particles/Tutorial Lecture, *Space Sci. Rev.*, *34*, 155–172, doi:10.1007/BF00194624.
Scarf, F. L., R. W. Fredricks, L. A. Frank, and M. Neugebauer (1971), Nonthermal electrons and high-frequency waves in the upstream solar wind, 1. Observations, *J. Geophys. Res.*, *76*, 5162–5171, doi:10.1029/JA076i022p05162.
Scarf, F. L., D. A. Gurnett, W. S. Kurth, and R. L. Poynter (1982), Voyager 2 plasma wave observations at Saturn, *Science*, *215*, 587–594, doi:10.1126/science.215.4532.587.
Sigsbee, K., C. A. Kletzing, D. A. Gurnett, J. S. Pickett, A. Balogh, and E. Lucek (2004), The dependence of Langmuir wave amplitudes on position in Earth's foreshock, *Geo. Res. Lett.*, *31*, L07805, doi:10.1029/2004GL019413.
Sigsbee, K., C. A. Kletzing, J. S. Pickett, D. A. Gurnett, S. J. Schwartz, B. Lefebvre, E. Lucek, A. N. Fazakerley, and H. Kucharek (2010), Characteristics of Langmuir electric field waveforms and power spectra exhibiting nonlinear behavior in Earth's foreshock, *J. Geophys. Res.*, *115*(A14), A10251, doi:10.1029/2009JA014948.
Smith, D. F., and D. Sime (1979), Origin of plasma-wave clumping in type III solar radio burst sources, *Astrophys. J.*, *233*, 998–1004, doi:10.1086/157463.

Soucek, J., T. Dudok, T. D. de Wit, V. Krasnoselskikh, and A. Volokitin (2003), Statistical analysis of nonlinear wave interactions in simulated Langmuir turbulence data, *Ann. Geophys.*, *21*, 681–692, doi:10.5194/angeo-21-681-2003.

Soucek, J., V. Krasnoselskikh, T. Dudok, T. D. de Wit, J. Pickett, and C. Kletzing (2005), Nonlinear decay of foreshock Langmuir waves in the presence of plasma inhomogeneities: Theory and Cluster observations, *J. Geophys. Res.*, *110*, A08102, doi:10.1029/2004JA010977.

Strangeway, R. J. (2004), Plasma waves and electromagnetic radiation at Venus and Mars, *Adv. Space Res.*, *33*, 1956–1967, doi:10.1016/j.asr.2003.08.040.

Strangeway, R. J., and G. K. Crawford (1995), VLF waves in the foreshock, *Adv. Space Res.*, *15*, 29–42.

Sulaiman, A. H., A. Masters, M. K. Dougherty, D. Burgess, M. Fujimoto, and G. B. Hospodarsky (2015), Quasiperpendicular high mach number shocks, *Phys. Rev. Lett.*, *115*(12), 125001, doi:10.1103/PhysRevLett.115.125001.

Voshchepynets, A., V. Krasnoselskikh, A. Artemyev, and A. Volokitin (2015), Probabilistic model of beam/plasma interaction in randomly inhomogeneous plasma, *Astrophys. J.*, *807*, 38, doi:10.1088/0004-637X/807/1/38.

Went, D. R., G. B. Hospodarsky, A. Masters, K. C. Hansen, and M. K. Dougherty (2011), A new semiempirical model of Saturn's bow shock based on propagated solar wind parameters, *J. Geophys. Res.*, *116*, A07202, doi:10.1029/2010JA016349.

Zimbardo, G., and P. Veltri (1996), Spreading and intermittent structure of the upstream boundary of planetary magnetic foreshocks, *Geophys. Res. Lett.*, *23*, 793–796, doi:10.1029/96GL00660.